Check for updates

A simple and accurate model for attenuation and dispersion caused by squirt flow in isotropic porous rocks

Yury Alkhimenkov[1] and Beatriz Quintal[2]

ABSTRACT

Seismic waves propagating in fluid-saturated porous rocks exhibit attenuation and velocity dispersion in a broad range of frequencies. At sonic and ultrasonic frequencies, the attenuation is predominantly caused by fluid flow in cracks and grain contacts, so-called squirt flow. This physical mechanism for attenuation also may be relevant at seismic frequencies. We develop a simple and accurate analytical model for attenuation and dispersion caused by squirt flow in isotropic porous rocks. The input material properties for a specific rock model can be directly measured in a laboratory or calculated using analytical and numerical approaches. The results from our squirt flow model are compared with inherently accurate 3D numerical solutions for the same pore geometries. The analytical and numerical results are in good agreement. Furthermore, we observe that our analytical model is more accurate than the currently available analytical solution for squirt flow in isotropic porous rocks. MATLAB routines to reproduce the presented results are made available.

INTRODUCTION

Seismic waves exhibit attenuation and velocity dispersion in a broad range of frequencies. Attenuation corresponds to the loss of the wave's energy during its propagation. Dispersion occurs associated with attenuation and corresponds to a change in the propagation velocity as a function of frequency. The nature of the energy loss might be elastic, e.g., scattering, or inelastic, for which energy is converted into heat. A major cause of inelastic attenuation in fluid-saturated rocks is wave-induced fluid flow (WIFF) at various scales. Because rocks are heterogeneous at several scales, the propagating seismic waves induce heterogeneous deformations. Such deformations in the fluid-saturated rock cause fluid pressure gradients, and as a result, dissipative fluid flow occurs until the fluid pressure equilibrates (Pride et al., 2004; Müller et al., 2010).

WIFF at the pore scale is known as squirt flow and, alone, this mechanism can cause strong energy dissipation and velocity dispersion in a broad range of frequencies. The first analytical studies of squirt flow were presented by Mavko and Nur (1975), O'Connell and Budiansky (1977), and Palmer and Traviolia (1980). Xu (1998), Chapman et al. (2002), Chapman (2003), and Jakobsen and Chapman (2009) incorporate the squirt flow mechanism into the effective medium theory formalism. Murphy et al. (1986), Mukerji and Mavko (1994), Dvorkin et al. (1995), Pride et al. (2004), Gurevich et al. (2010), Collet and Gurevich (2016), Glubokovskikh et al. (2016), and Alkhimenkov and Quintal (2022a, 2022b) study squirt flow between interconnected compliant cracks and stiff pores. In recent years, laboratory investigations of elastic moduli dispersion and attenuation based on the forced oscillation method have yielded measurements of attenuation over a broad and well-sampled array of frequencies, thus measuring the detailed frequency-dependent behavior of attenuation and dispersion caused by squirt flow (Pimienta et al., 2015a, 2015b; Subramaniyan et al., 2015; Borgomano et al., 2019; Chapman et al., 2019; Sun et al., 2020). Analytical solutions are useful for the interpretation of these frequency-dependent measurements, allowing for a quantitative analysis of the effects associated with this physical mechanism (Chapman et al., 2019).

Recently, numerical solutions were proposed and used to study seismic wave attenuation and dispersion due to squirt flow (Zhang et al., 2010; Zhang and Toksöz, 2012; Quintal et al., 2016, 2019; Das et al., 2019; Lissa et al., 2020, 2021). Based on the approach suggested by Quintal et al. (2019), Alkhimenkov et al. (2020a) compare accurate numerical solutions against the published analyti-

[1]Formerly University of Lausanne, Institute of Earth Sciences, Lausanne, Switzerland; presently Massachusetts Institute of Technology, Department of Civil and Environmental Engineering, Cambridge, Massachusetts, USA and Lomonosov Moscow State University, Faculty of Mechanics and Mathematics, Moscow, Russia. E-mail: yalkhime@mit.edu (corresponding author).
[2]University of Lausanne, Institute of Earth Sciences, Lausanne, Switzerland. E-mail: beatriz.quintal@unil.ch.

cal model for squirt flow in anisotropic porous rocks by Collet and Gurevich (2016) for the exact same pore geometry and observe significant discrepancies between numerical and analytical results. Based on the understanding obtained in such a numerical study, Alkhimenkov and Quintal (2022a) propose a new analytical model for squirt flow in anisotropic porous rocks for the classical pore geometry corresponding to a toroidal pore connected to a crack. Then, Alkhimenkov and Quintal (2022b) extend this model to deal with more realistic geometries of the pore space corresponding to a crack connected to one or multiple spherical pores. These analytical models were all in good agreement with accurate numerical solutions for the same pore geometries. Validation of analytical models against numerical solutions for the same proposed geometry is of great importance because it delineates the accuracy and the range of validity of the analytical model. The models of Alkhimenkov and Quintal (2022a, 2022b) provide solutions to anisotropic scenarios considering a single crack, which has limited applicability to rocks containing aligned cracks. Therefore, the next natural and important step is to develop an analytical model for isotropic rocks containing randomly oriented cracks.

In this study, the analytical model proposed by Alkhimenkov and Quintal (2022b) for seismic attenuation and dispersion caused by squirt flow is extended to isotropic rocks. The analytical model has a simple form and is validated against inherently accurate 3D numerical solutions for the same pore geometry. A comparison against the published analytical model for squirt flow in isotropic rocks by Gurevich et al. (2010) also is shown. Our model considers pore geometries that are more realistic than those considered in the analytical model of Gurevich et al. (2010), which allows us to better understand and identify the geometric properties of the pore space that control squirt flow. MATLAB routines that can be used to reproduce the presented results are available from a permanent DOI repository (Zenodo) (Alkhimenkov and Quintal, 2023).

THE ANALYTICAL MODEL

Here, we extend the analytical model presented by Alkhimenkov and Quintal (2022b) to isotropic rocks.

Attenuation and dispersion due to squirt flow

We use the inverse quality factor $1/Q(\omega)$ as a measure of seismic P-wave attenuation (O'Connell and Budiansky, 1978):

$$\frac{1}{Q(\omega)} = \frac{\text{Im}(M(\omega))}{\text{Re}(M(\omega))}, \qquad (1)$$

where $\omega = 2\pi f$ is the angular frequency, f is the linear frequency, $M = K + 4/3G$ is the complex-valued P-wave modulus, and K and G are the bulk and shear moduli, respectively. Squirt flow causes attenuation and corresponding dispersion of the stiffness moduli. Due to the dispersion of, for example, the P-wave modulus, velocity dispersion will be observed in a propagating P wave.

A rock is parameterized by three components: solid elastic matrix (grains), isometric stiff pores, and thin compliant cracks. Pores and cracks are interconnected and saturated with a fluid. The total porosity ϕ is represented by the sum of the stiff porosity ϕ_s and the compliant porosity ϕ_c:

$$\phi = \phi_s + \phi_c. \qquad (2)$$

Because $\phi_c \ll \phi_s$, one can assume that $\phi \approx \phi_s$.

Low frequencies

At low frequencies, there is sufficient time for fluid pressure equilibration between cracks and pores resulting in a uniform pressure distribution in the rock. This is usually referred to as a relaxed state. The effective elastic moduli of a fluid-saturated rock in this relaxed state (K_{low}, G_{low}) are given by Gassmann's equations (Gassmann, 1951; Alkhimenkov, 2023), respectively,

$$K_{\text{low}} = \left[\frac{1}{K_g} + \frac{\phi(1/K_f - 1/K_g)}{1 + \phi(1/K_f - 1/K_g)(1/K_{\text{dry}} - 1/K_g)^{-1}}\right]^{-1} \qquad (3)$$

and

$$G_{\text{low}} = G_{\text{dry}}, \qquad (4)$$

where K_{dry} and G_{dry} are the bulk and shear moduli of a dry rock, respectively; K_f is the fluid bulk modulus; and K_g is the bulk modulus of solid grains.

High frequencies

At high frequencies, there is no time for fluid pressure equilibration between cracks and pores; therefore, cracks behave as hydraulically isolated. This is usually referred to as an unrelaxed state. To quantify this effect, we consider the modified frame concept (Mavko and Jizba, 1991), in which the cracks are saturated with a fluid, whereas the isometric pores remain empty. The unrelaxed (high-frequency) effective elastic moduli of the modified frame are given by Mavko-Jizba relations (Mavko and Jizba, 1991). Mavko-Jizba relations are generalized by Gurevich et al. (2009)

$$K_{uf} = \left[\frac{1}{K_h} + \frac{1}{(1/K_{\text{dry}} - 1/K_h)^{-1} + (\phi_c(1/K_f - 1/K_g))^{-1}}\right]^{-1}, \qquad (5)$$

$$G_{uf} = \left[\frac{1}{G_{\text{dry}}} - \frac{4}{15}\left(\frac{1}{K_{\text{dry}}} - \frac{1}{K_{uf}}\right)\right]^{-1}, \qquad (6)$$

where K_h is the bulk modulus of a rock without compliant porosity. The bulk and shear moduli of a fully saturated rock at high frequencies (K_{high}, G_{high}) are then calculated from K_{uf} and G_{uf} using Gassmann's equations (Gassmann, 1951; Alkhimenkov, 2023), respectively,

$$K_{\text{high}} = \left[\frac{1}{K_g} + \frac{\phi_s(1/K_f - 1/K_g)}{1 + \phi_s(1/K_f - 1/K_g)(1/K_{uf} - 1/K_g)^{-1}}\right]^{-1} \qquad (7)$$

and

$$G_{\text{high}} = G_{uf}. \tag{8}$$

Intermediate frequencies

At intermediate frequencies, a transition from low-frequency (relaxed) moduli to high-frequency (unrelaxed) moduli takes place. The cause of such frequency-dependent rock moduli and the corresponding attenuation is the fluid pressure diffusion in compliant cracks. The exact shapes of the attenuation and dispersion curves due to squirt flow at intermediate frequencies can be obtained numerically and will be different for different pore-space configurations (Alkhimenkov and Quintal, 2022a, 2022b). Moreover, an analytical approximation is proposed in this study and the resulting expressions are given next.

Workflow of the analytical model

The workflow of the present analytical model consists of three steps as in Alkhimenkov and Quintal (2022b) and is shown in Figure 1 as follows:

1) First, we obtain the moduli of a dry rock (K_{dry}, G_{dry}) and the moduli of a rock without compliant porosity (K_h).
2) Second, the frequency-dependent moduli of the partially relaxed modified frame ($K_{\text{mf}}(\omega)$, $G_{\text{mf}}(\omega)$) are obtained by using the crack stiffness relaxation function due to squirt flow.
3) Finally, the moduli of the fully saturated rock ($K_{\text{sat}}(\omega)$, $G_{\text{sat}}(\omega)$) are obtained by applying Gassmann's equations (Gassmann, 1951; Alkhimenkov, 2023) at each frequency.

Step 1: Moduli of the dry rock

The moduli of a dry rock and the moduli of a rock without compliant porosity can be calculated analytically, numerically, or measured in laboratory. However, there is no approach to calculate analytically the effective elastic properties of a model with interconnected pores and cracks in three dimensions exactly. One approach to approximate the effective properties of a model with interconnected pores and cracks using the compliance contribution tensors (Nemat-Nasser and Hori, 2013; Kachanov and Sevostianov, 2018) was presented by Alkhimenkov and Quintal (2022a, 2022b). It is important to note that the interconnectivity of stiff pores and compliant cracks is a key factor in the calculation of the dry moduli of the model.

The compliance of cracks can be calculated as (Gurevich et al., 2009)

$$\overline{Z}_N^{\text{dry}} = \frac{1}{K_{\text{dry}}} - \frac{1}{K_h}, \tag{9}$$

where $\overline{Z}_N^{\text{dry}}$ is the average normal compliance of all dry cracks. Due to the connectivity of cracks to stiff pores, this compliance might be twice as large (for the considered pore geometry) than that in the case in which cracks are isolated (Alkhimenkov and Quintal, 2022a, 2022b). However, this effect depends on the pore geometry.

The moduli of a dry rock also can be measured in laboratory. In this case, the moduli of a rock without compliant porosity approximately correspond to conditions under effective pressures that are sufficiently high so that the measurements become nearly pressure independent due to a presumed closure of cracks (Shapiro, 2003; Morozov and Deng, 2018).

Step 2: Frequency-dependent moduli of the modified frame

At intermediate frequencies, a transition from the relaxed to unrelaxed state occurs. A tool to describe this transition is the concept of the modified frame moduli, in which the pores are dry but cracks are fully saturated. Squirt flow takes place in compliant cracks; therefore, they are responsible for the frequency-dependent rock properties. Alkhimenkov and Quintal (2022b) suggest that squirt flow can be approximated by the following 1D equation for fluid pressure p under the strain ϵ_c applied to the walls of the 1D crack:

$$\frac{\partial^2 p}{\partial x^2} - k^2 p = -k^2 K_f \epsilon_c, \tag{10}$$

where

$$k = \frac{2}{h} \sqrt{3 i \omega \eta / \left(K_f + \frac{4}{3} i \omega \eta \right)} \tag{11}$$

is a function of the rheology of the crack (Tsai and Lee, 1998), and h is the crack aperture. The boundary condition is set to zero stress at $x = \pm l^{\text{sq}}$, which are boundaries of the 1D layer (the length l^{sq} is equivalent to the radius of the crack). To obtain the frequency-dependent fluid bulk modulus, the elastic-viscoelastic correspondence principle is used (Hashin, 1970), with the full derivation given as supplementary material in Alkhimenkov and Quintal (2022b). The solution is
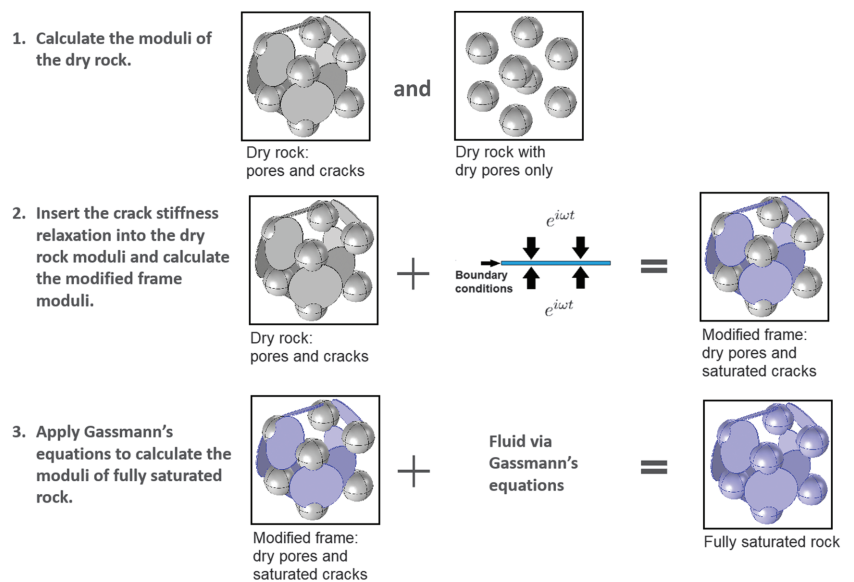
Figure 1. Sketch illustrating the workflow of the present analytical model (modified after Alkhimenkov and Quintal, 2022a).

$$K_f^*(\omega) = K_f + \frac{4}{3} i\omega\eta - \frac{(K_f - \frac{2}{3} i\omega\eta)^2}{(K_f + \frac{4}{3} i\omega\eta)} \frac{\tanh(\bar{k}_3)}{\bar{k}_3}, \quad (12)$$

where η is the shear viscosity of the fluid and

$$\bar{k}_3 = \frac{1}{\alpha} \sqrt{3 i\omega\eta / \left(K_f + \frac{4}{3} i\omega\eta \right)}, \quad (13)$$

where $\alpha = h/(2l^{sq})$ is the crack aspect ratio. Note that solution 12 also can be derived from the results presented by Tsai and Lee (1998) using the same elastic-viscoelastic correspondence principle (Hashin, 1970). Note that we consider fluid pressure diffusion in one dimension while Gurevich et al. (2010) and Glubokovskikh et al. (2016) consider radial fluid pressure diffusion; thus, their equations for $K_f^*(\omega)$ are different.

The frequency-dependent crack stiffness can now be calculated by considering the frequency-dependent bulk modulus of the fluid $K_f^*(\omega)$ (expression 12). By substituting $K_f^*(\omega)$ into equation 5, the expression for the frequency-dependent bulk and shear moduli of the modified frame can be written as, respectively,

$$K_{mf}(\omega)$$
$$= \left[\frac{1}{K_h} + \frac{1}{(1/K_{dry} - 1/K_h)^{-1} + (\phi_c (1/K_f^*(\omega) - 1/K_g))^{-1}} \right]^{-1}, \quad (14)$$

$$G_{mf}(\omega) = \left[\frac{1}{G_{dry}} - \frac{4}{15} \left(\frac{1}{K_{dry}} - \frac{1}{K_{mf}(\omega)} \right) \right]^{-1}. \quad (15)$$

Step 3: Moduli of the fully saturated rock

The moduli of a fully saturated rock can be calculated through Gassmann's equations (Gassmann, 1951; Alkhimenkov, 2023) using the bulk modulus of the modified frame, obtained from equation 14 at each frequency:

$$K_{sat}(\omega)$$
$$= \left[\frac{1}{K_g} + \frac{\phi_s (1/K_f - 1/K_g)}{1 + \phi_s (1/K_f - 1/K_g)(1/K_{mf}(\omega) - 1/K_g)^{-1}} \right]^{-1}, \quad (16)$$

$$G_{sat}(\omega) = \left[\frac{1}{G_{dry}} - \frac{4}{15} \left(\frac{1}{K_{dry}} - \frac{1}{K_{mf}(\omega)} \right) \right]^{-1}. \quad (17)$$

Expressions 12, 14, 16, and 17 represent the complete solution of the present analytical model. The velocity dispersion and attenuation of P and S waves propagating through such a porous model can be calculated from the complex stiffness moduli given in equations 16 and 17.

NUMERICAL VALIDATION

Numerical methodology

To validate the analytical model, 3D numerical solutions are obtained for the same pore geometries that are assumed in the analytical model. At the pore scale, a rock is represented by grains (solid phase) and a fluid-saturated pore space. The solid phase is described as a linear isotropic elastic material for which the conservation of momentum is

$$\nabla \cdot \boldsymbol{\sigma} = 0, \quad (18)$$

where $\boldsymbol{\sigma}$ is the stress tensor and $\nabla \cdot$ denotes the divergence operator acting on the stress field $\boldsymbol{\sigma}$. The stress-strain relation is

$$\boldsymbol{\sigma} = \mathbf{C} : \boldsymbol{\epsilon}, \quad (19)$$

where $\boldsymbol{\epsilon}$ is the strain tensor, $\mathbf{C}$ is the fourth rank stiffness tensor, and : denotes the double dot product. For an isotropic solid material, the components of the stiffness tensor can be fully described by the bulk K and shear G moduli. The fluid phase is described by the quasi-static linearized compressible Navier-Stokes momentum equation (Landau and Lifshitz, 1959):

$$-\nabla p + \eta\nabla^2\mathbf{v} + \frac{1}{3}\eta\nabla(\nabla \cdot \mathbf{v}) = 0, \quad (20)$$

where $\mathbf{v}$ is the fluid velocity, p is the fluid pressure, η is the shear viscosity, and ∇ denotes the nabla operator acting on the vector $\mathbf{v}$ and scalar p fields. Equation 20 is valid for the laminar flow of a Newtonian fluid at low Reynolds numbers (R_e, $R_e < 1$).

In our numerical solution, equations 19 and 20 are combined together resulting in one expression (Quintal et al., 2016, 2019), accompanied by a generalized stress-strain relation in the space-frequency domain written here in index form as

$$\sigma_{ij} = \lambda e \delta_{ij} + 2G\epsilon_{ij} + i\omega \left(2\eta\epsilon_{ij} - \frac{2}{3} \eta e \delta_{ij} \right), \quad (21)$$

where ϵ_{ij} is the components of the strain tensor,

$$\epsilon_{ij} = \frac{1}{2} \left(\frac{\partial u_i}{\partial x_j} + \frac{\partial u_j}{\partial x_i} \right). \quad (22)$$

Here, e is the trace of the strain tensor, λ and G are the Lame parameters, u_i denotes the displacement in the ith direction, and δ_{ij} is the Kronekecker delta. Equations 18 and 21 are implemented with a finite-element solver. In the domain of the model representing a solid material, equation 21 reduces to equation 19 by setting the shear viscosity η to zero. Similarly, in the domain of the model representing a compressible viscous fluid, the shear modulus μ is set to zero; hence, equations 21 and 18 reduce to the linearized compressible Navier-Stokes equation 20. An advantage of the proposed formulation is the natural coupling between the solid and fluid displacements at the boundaries between subdomains (Quintal et al., 2016).

Direct relaxation tests are performed to compute P-wave (M), bulk (K), and shear (G) moduli, along with the corresponding attenuation. A displacement boundary condition of the form $u = 10^{-8} \times \exp(i\omega t)$ is applied to a certain external wall(s) of the cubic model and in a certain direction, whereas at other walls

of the model, the displacements are set to zero or left free to change. A detailed explanation of the boundary conditions is given in Alkhimenkov et al. (2020a, 2020b). The resulting stress is averaged to calculate the complex moduli of the homogenized viscoelastic material (Jänicke et al., 2015). For example, the complex P-wave modulus $M(\omega)$ is calculated as

$$M(\omega) = \frac{\langle \sigma_{33}(\omega) \rangle}{\langle \epsilon_{33}(\omega) \rangle}, \tag{23}$$

where $\langle \cdot \rangle$ represents the volume average over the model domain. Then, P-wave attenuation is calculated using this result and the definition given in equation 1.

Because the analytical models are derived for isotropic rocks, the numerical simulations are performed for special geometries that are nearly isotropic. Two different models are considered (Figure 2). The elastic solid grain material in these models is represented by a cube with dimensions of 0.44 m × 0.44 m × 0.44 m. To achieve isotropic symmetry, a total of nine cracks are modeled in these models, divided into three groups. Each group consists of three cracks with the angle of 60° to each other, which gives isotropy in the corresponding 2D plane. Then, each group is rotated to make an isotropic configuration in three 2D planes (XY, XZ, and YZ). In model 1, the stiff pores are represented only by spheres, whereas in model 2, they are represented by spheres and cylinders. The material parameters used in this study are shown in Table 1. The properties of the solid material are those of quartz and the fluid properties are those of glycerin. The latter is frequently used to saturate the rock sample in laboratory experiments due to is high viscosity. The geometric properties of the pore space are provided in Table 2. The geometry in all models is scalable, which means that the numerical solution remains unchanged if all the geometric properties are rescaled by any factor. In other words, the absolute dimensions are meaningless; only the relative dimensions are relevant. The numerical discretization of model 1 using an unstructured finite-element mesh is shown in Appendix A.
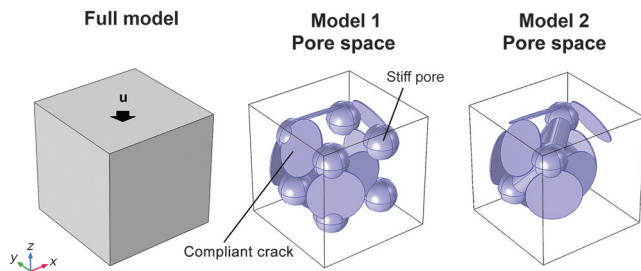
Figure 2. Sketch illustrating the the geometries of the pore space in models 1 and 2. The displacement boundary condition $u = 10^{-8} \times \exp(i\omega t)$ is applied to the top boundary of the model to calculate the P-wave modulus $M = K + 4/3G$.

Table 1. Material properties, which are the same for the two models.

Material parameter	Solid	Fluid
Bulk modulus K	36 GPa	4.3 GPa
Shear modulus G	44 GPa	0 GPa
Shear viscosity η	0 Pa·s	1.414 Pa·s

Model 1

In model 1, the stiff pores are represented by spheres only. Eight pores are considered in total. Nine cracks are connected to the pores. Three cracks have four connections to pores, and six cracks have two connections to pores (Figure 2). Figure 3 shows the results for the modified frame obtained with the present analytical model, the analytical model from Gurevich et al. (2010), and the numerical solution. Our analytical model is in good agreement with the numerical solution. The model presented by Gurevich et al. (2010) is shifted to higher frequencies because it considers radial flow in the crack toward a toroidal pore. The characteristic frequency of the fluid pressure relaxation in the case of radial flow is slightly higher than in 1D flow (Alkhimenkov and Quintal, 2022a), which is the case for our model and explains the difference observed in Figure 3.

Table 2. Geometric properties for the two models.

Geometric parameter	Model 1	Model 2
Flat cylinder (crack) radius, b (m)	0.1	0.1
Flat cylinder (crack) thickness, h (m)	0.004	0.004
Crack aspect ratio, $\alpha = h/(2b)$	0.02	0.02
Radius of the spherical pores (m)	0.0625	0.0625, ≈ 0.0952
Pore volume (cracks and pores) (m^3)	≈ 0.009181	≈ 0.010089
Total porosity	≈ 0.1078	≈ 0.1184
Crack porosity	≈ 0.0122	≈ 0.0128
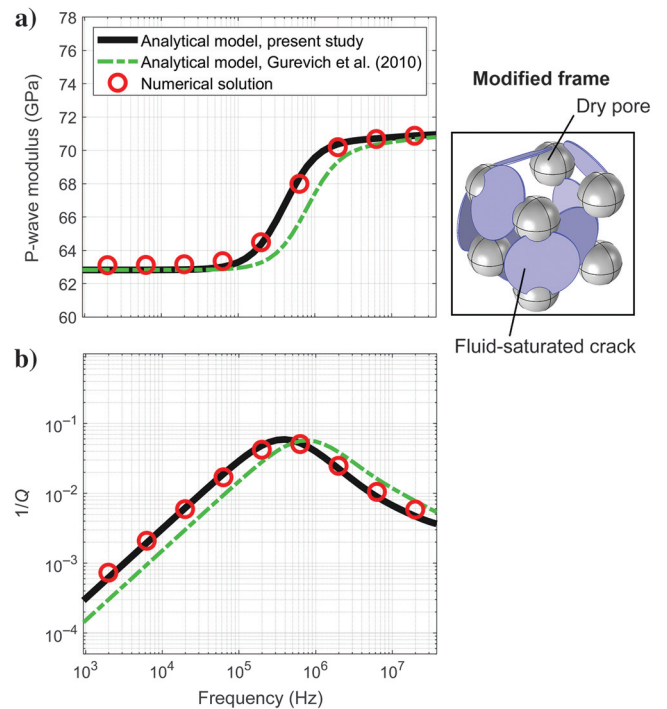
Figure 3. Numerical and analytical results for the modified frame of model 1: (a) real part of the P-wave modulus $M(\omega) = K(\omega) + 4/3G(\omega)$ and (b) corresponding dimensionless attenuation.

Figure 4 shows the results for the fully saturated model obtained with the present analytical model, the analytical model from Gurevich et al. (2010), and the numerical solution. The results from our analytical model are in good agreement with the numerical solution. Again, a similar difference can be observed in characteristic frequencies between the numerical solution and the analytical model presented by Gurevich et al. (2010).

For the fully saturated numerical model, Figure 5 shows snapshots of the fluid pressure field at three different frequencies: at a very low frequency, at the characteristic frequency (f_c), and at a very high frequency. At a very low frequency, the pore pressure is homogeneous representing the relaxed state. At the characteristic frequency, maximum fluid pressure gradients are observed and fluid flow takes place between the crack and the pore. At a very high frequency, fluid pressure is high in the crack and low in the pore, corresponding to a scenario in which the crack behaves as if it was hydraulically isolated.
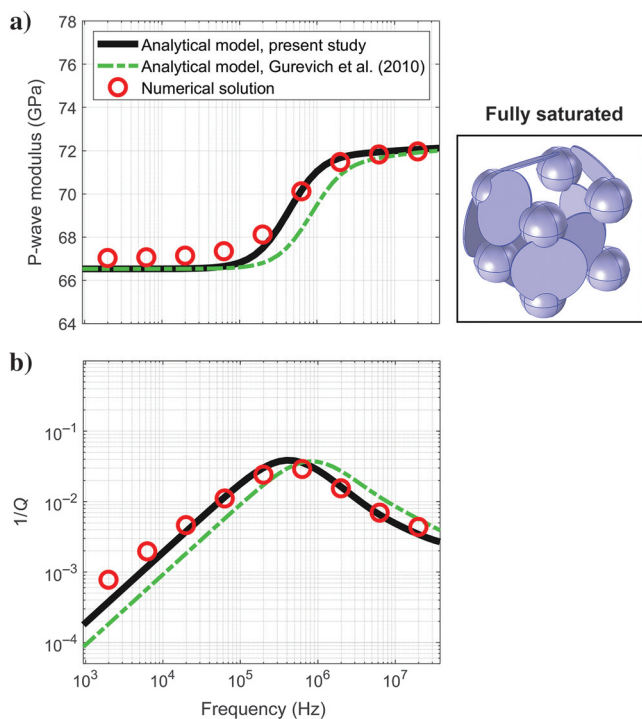
Figure 4. Numerical and analytical results for the fully saturated model 1: (a) real part of the P-wave modulus $M(\omega) = K(\omega) + 4/3G(\omega)$ and (b) corresponding dimensionless attenuation.
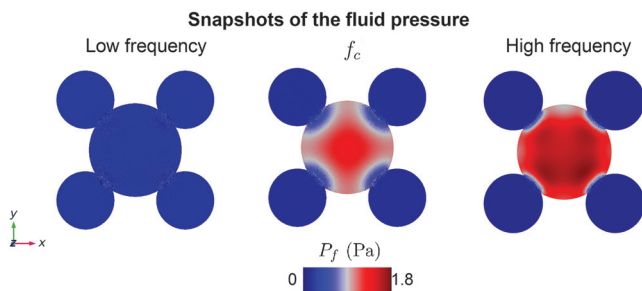
Figure 5. Snapshots of the fluid pressure field in a horizontal slice of the fully saturated model 1 at very low frequency, the characteristic frequency (f_c), and very high frequency.

Model 2

In model 2, the stiff pores are represented by four spheres and three cylinders. Nine cracks are connected to the pores. Each crack has only one connection to a spherical pore, and the spherical pores are connected to cylindrical pores (Figure 2). Figure 6 shows the results for the modified frame obtained with the present analytical model, the analytical model presented by Gurevich et al. (2010), and the numerical solution. The geometry of model 2 is slightly anisotropic; therefore, the discrepancy between the numerical solution and the present analytical model for isotropic rocks might be larger than observed for model 1. Yet, the present analytical model is in good agreement with the numerical solution. The corresponding model by Gurevich et al. (2010) is significantly shifted to higher frequencies.

Figure 7 shows the results for the fully saturated model obtained with the present analytical model, the analytical model presented by Gurevich et al. (2010), and the numerical solution. The present analytical model is in good agreement with the numerical solution. Again, a big discrepancy is visible in characteristic frequencies between the numerical solution and the analytical model presented by Gurevich et al. (2010). This discrepancy in characteristic frequencies, as well as that observed in Figure 6, will be explained in the next section.

DISCUSSION

The squirt flow aspect ratio α^{sq}

Figure 8 shows the definition of the squirt flow length l^{sq} for the two models. The squirt flow length l^{sq} is the distance between two
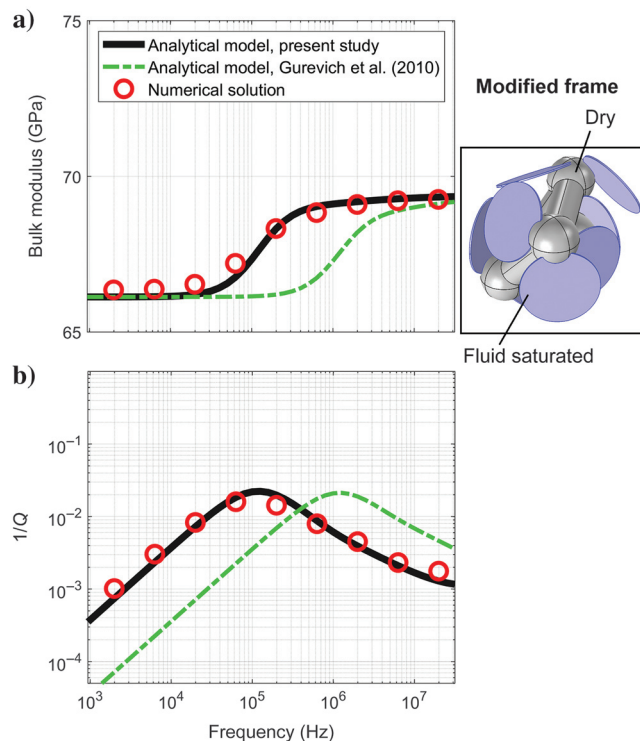
Figure 6. Numerical and analytical results for the modified frame of model 2: (a) real part of the P-wave modulus $M(\omega) = K(\omega) + 4/3G(\omega)$ and (b) corresponding dimensionless attenuation.

points within a crack along which the squirt flow occurs (p1p2, p3p4, p3p5, and p7p6). One point might be the most distant point in the crack from the pore(s). The other point corresponds to the connection of the crack to the pore. The squirt flow thickness h^{sq} is the crack aperture. Finally, the parameter controlling the characteristic frequency is the squirt flow aspect ratio α^{sq} (Alkhimenkov and Quintal, 2022b):

$$\alpha^{sq} = \frac{1}{2}\frac{h^{sq}}{l^{sq}}. \tag{24}$$

There are two different squirt flow lengths in model 1. Three cracks provide us with $p1p2 \approx 0.9b$, and six other cracks provide us with $p3p4 = p3p5 \approx 0.8\sqrt{3}b$. By simple arithmetic averaging, the squirt flow length in model 1 is

$$l^{sq}_{m1} \approx (2(0.8\sqrt{3}b) + 0.9b)/3 \approx 0.0877. \tag{25}$$

In model 2, only one squirt flow length is present (p7p6):

$$l^{sq}_{m2} \approx 2b = 0.2. \tag{26}$$

Note that the squirt flow length in model 2 is approximately twice that in the model 1. More precisely,

$$\frac{l^{sq}_{m2}}{l^{sq}_{m1}} = 2.28. \tag{27}$$

This ratio is responsible for the dramatic difference in the characteristic frequencies between two models (Figures 6 and 7). In other words, the crack aspect ratio is not the key parameter that controls the characteristic frequency of squirt flow. Instead, the squirt flow aspect ratio controls the characteristic frequency of squirt flow. In model 1, the squirt flow length is approximately the radius of the crack; however, in model 2, the squirt flow length l^{sh} is approximately the diameter of the crack. The difference by a factor of two approximately corresponds to the shift in the characteristic frequency by one order of magnitude. The resulting characteristic frequency of squirt flow ω_c can be rewritten as

$$\omega_c \approx \frac{2\pi K_{dry}}{\eta}(\alpha^{sq})^3. \tag{28}$$

Maximum gradients in fluid pressure occur at the characteristic frequency (Figure 9). In model 1, the maximum fluid pressure gradients occur from the center of the crack to the connection of the crack to the pore (Figure 9a), which corresponds to the squirt flow length. Instead, in model 2, the maximum fluid pressure gradients occur along the diameter of the crack, which corresponds to the squirt flow length (Figure 9b).

The characteristic frequency of the analytical model presented by Gurevich et al. (2010) is a function of the crack aspect ratio and assumes radial fluid flow in the crack, which is connected to a toroidal pore. Therefore, for models 1 and 2, their analytical model predicts the same characteristic frequency. The shapes of
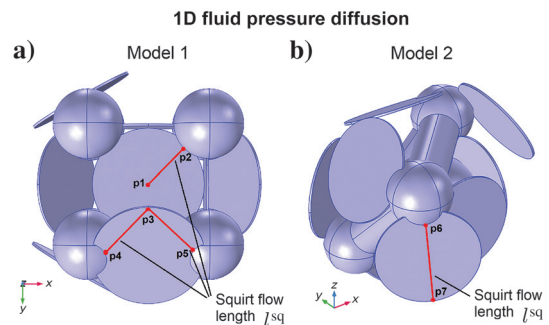
Figure 8. Sketch illustrating the definition of the squirt flow length l^{sq} for models 1 and 2.

Figure 7. Numerical and analytical results for the fully saturated model 2: (a) real part of the P-wave modulus $M(\omega) = K(\omega) + 4/3G(\omega)$ and (b) corresponding dimensionless attenuation.
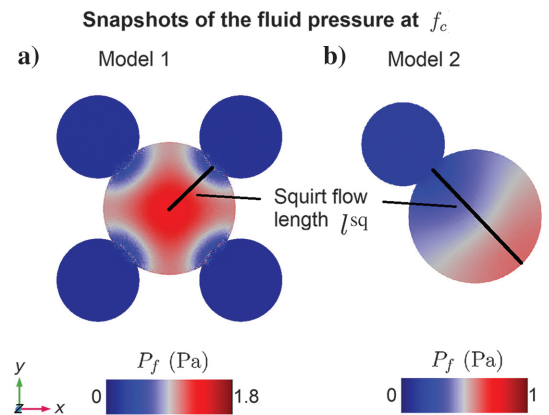
Figure 9. Snapshots of the fluid pressure field at the characteristic frequency f_c in a horizontal slice of the models illustrating the definition of the squirt flow length l^{sq}.

the dispersion and attenuation curved of the analytical model presented by Gurevich et al. (2010) also are slightly different from the present model due to the different pore geometry (Alkhimenkov and Quintal, 2022a).

Comparison against previous models

The present model has several key differences from the previous models published by Gurevich et al. (2010) and Glubokovskikh et al. (2016). Here, we use a model for 1D flow, whereas Gurevich et al. (2010) and Glubokovskikh et al. (2016) use a model for radial flow. This is a significant improvement because it allows for flow in the crack toward individual spherical pores rather than toward a toroidal pore. As shown by Alkhimenkov and Quintal (2022b), the used 1D flow model is appropriate for a partial contact between the tip of a crack and one or multiple spherical pores and agrees well with the numerical solution for that geometry. This geometry is clearly more realistic that with a toroidal pore considered by Murphy et al. (1986), Gurevich et al. (2010), Glubokovskikh et al. (2016), and Alkhimenkov and Quintal (2022a). Furthermore, the presented model is based on the squirt flow length concept, which can accurately describe a particular fluid flow path within the crack and thus the characteristic frequency. Previous models (Gurevich et al., 2010; Glubokovskikh et al., 2016) considered the crack aspect ratio as the main parameter that controls the characteristic frequency of squirt flow. Detailed comparisons between the anisotropic version of the presented analytical model and previous models are given by Alkhimenkov and Quintal (2022a, 2022b).

Figure 10. Numerical results for the modified frame and the fully saturated model 1: (a) real part of the shear modulus $G(\omega)$ and (b) corresponding dimensionless attenuation.

Dispersion of shear modulus

Mavko and Jizba (1991) and Gurevich et al. (2010) assume that the frequency-dependent shear modulus of the modified frame is equal to the shear modulus of a fully saturated rock,

$$G_{\text{sat}}(\omega) = G_{\text{mf}}(\omega). \qquad (29)$$

Figure 10 shows the numerical results for the shear modulus of the modified frame and of the fully saturated model 1. The numerical solutions are in reasonably good agreement, confirming the validity of the proposed assumption.

Importance for laboratory measurements

The present analytical model, compared with previous models, is dependent on a different parameter, the so-called squirt flow aspect ratio $\alpha^{\text{sq}} = h^{\text{sq}}/(2l^{\text{sq}})$. The squirt flow length l^{sq} describes the 1D fluid pressure diffusion in the crack and is different in models 1 and 2 by a factor of ≈ 2. The squirt flow aperture h^{sq} is the crack aperture. The new parameter α^{sq} can precisely describe the characteristic frequency of squirt flow, which might not be the case for the crack aspect ratio. Even though the squirt flow aspect ratio cannot be easily measured in real rocks (but neither can the crack aspect ratio), it could be estimated based on the knowledge of the pore geometry from microscopic images of the rock sample. Furthermore, in real rocks, the crack aperture varies due to asperities and Lissa et al. (2020) show that, for such cases, the minimum value of the crack aperture should be used.

A more accurate analytical model should yield more accurate interpretations of frequency-dependent measurements of squirt flow in the laboratory and thus can allow for a deeper understanding of this physical mechanism.

CONCLUSION

We have developed a simple and accurate analytical model for seismic dispersion and attenuation caused by squirt flow in isotropic porous rocks. The model is consistent with Gassmann's equations at low frequencies and Mavko-Jizba relations at high frequencies. The analytical model is validated against inherently accurate 3D numerical solutions for the same pore geometries, with excellent agreement. The input parameters for the model can be measured in the laboratory, calculated analytically, or numerically. Compared with previous models, a new parameter is introduced, the squirt flow aspect ratio, which is the crack aperture divided by twice the squirt flow length. The squirt flow length is related to the geometric pressure diffusion pattern within the crack, which might be significantly different for different pore geometries. Thus, the squirt flow aspect ratio accurately controls the characteristic frequency of squirt flow, which might not be the case for the crack aspect ratio used in previous squirt flow analytical models. For example, in different pore geometries with the same crack aspect ratio, the different squirt flow aspect ratios might lead to a difference of an order of magnitude among the characteristic frequencies, which we also demonstrated numerically.

The full model   The pore space   The pore space (magnified)   The pore space (magnified)
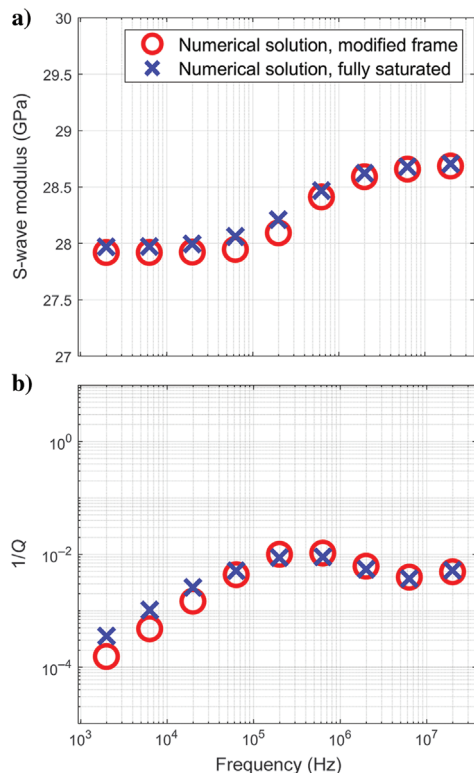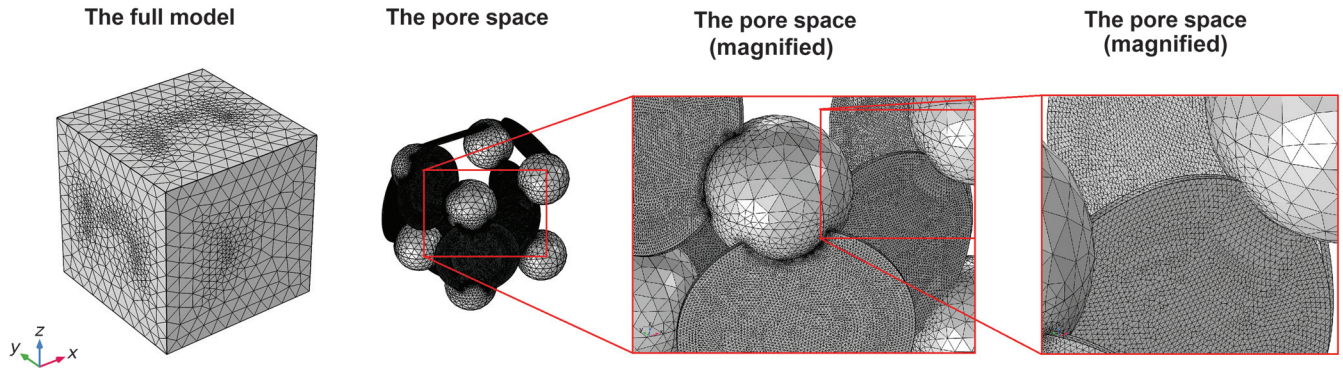
Figure A-1. Sketch illustrating the numerical mesh used for the spatial discretization of model 1.

DATA AND MATERIALS AVAILABILITY

No data have been required for this paper.

APPENDIX A

NUMERICAL DISCRETIZATION

Figure A-1 shows the numerical discretization of the model 1. The total number of elements is 1.29×10^6 in each simulation. The mesh is very fine in the crack to accurately capture the fluid pressure diffusion and coarse in the stiff pores and solid grains.

REFERENCES

Alkhimenkov, Y., 2023, Numerical validation of Gassmann's equations: Geophysics, **88**, no. 4, A25–A29, doi: 10.1190/geo2023-0023.1.

Alkhimenkov, Y., E. Caspari, B. Gurevich, N. D. Barbosa, S. Glubokovskikh, J. Hunziker, and B. Quintal, 2020a, Frequency-dependent attenuation and dispersion caused by squirt flow: Three-dimensional numerical study: Geophysics, **85**, no. 3, MR129–MR145, doi: 10.1190/geo2019-0519.1.

Alkhimenkov, Y., E. Caspari, S. Lissa, and B. Quintal, 2020b, Azimuth-, angle- and frequency-dependent seismic velocities of cracked rocks due to squirt flow: Solid Earth, **11**, 855–871, doi: 10.5194/se-11-855-2020.

Alkhimenkov, Y., and B. Quintal, 2023, Analytical model for attenuation and dispersion caused by squirt flow in isotropic porous rocks (1.0): Zenodo, doi: 10.5281/zenodo.8266275.

Alkhimenkov, Y., and B. Quintal, 2022a, An accurate analytical model for squirt flow in anisotropic porous rocks — Part 1: Classical geometry: Geophysics, **87**, no. 2, MR85–MR103, doi: 10.1190/geo2021-0229.1.

Alkhimenkov, Y., and B. Quintal, 2022b, An accurate analytical model for squirt flow in anisotropic porous rocks — Part 2: Complex geometry: Geophysics, **87**, no. 6, MR291–MR302, doi: 10.1190/geo2022-0143.1.

Borgomano, J. V., L. X. Pimienta, J. Fortin, and Y. Guéguen, 2019, Seismic dispersion and attenuation in fluid-saturated carbonate rocks: Effect of microstructure and pressure: Journal of Geophysical Research: Solid Earth, **124**, 12498–12522, doi: 10.1029/2019JB018434.

Chapman, M., 2003, Frequency-dependent anisotropy due to meso-scale fractures in the presence of equant porosity: Geophysical Prospecting, **51**, 369–379, doi: 10.1046/j.1365-2478.2003.00384.x.

Chapman, M., S. V. Zatsepin, and S. Crampin, 2002, Derivation of a microstructural poroelastic model: Geophysical Journal International, **151**, 427–451, doi: 10.1046/j.1365-246X.2002.01769.x.

Chapman, S., J. V. Borgomano, H. Yin, J. Fortin, and B. Quintal, 2019, Forced oscillation measurements of seismic wave attenuation and stiffness moduli dispersion in glycerine-saturated Berea sandstone: Geophysical Prospecting, **67**, 956–968, doi: 10.1111/1365-2478.12710.

Collet, O., and B. Gurevich, 2016, Frequency dependence of anisotropy in fluid saturated rocks — Part I: Aligned cracks case: Geophysical Prospecting, **64**, 1067–1084, doi: 10.1111/1365-2478.12384.

Das, V., T. Mukerji, and G. Mavko, 2019, Numerical simulation of coupled fluid-solid interaction at the pore scale: A digital rock-physics technology: Geophysics, **84**, no. 4, WA71–WA81, doi: 10.1190/geo2018-0488.1.

Dvorkin, J., G. Mavko, and A. Nur, 1995, Squirt flow in fully saturated rocks: Geophysics, **60**, 97–107, doi: 10.1190/1.1443767.

Gassmann, F., 1951, Über die elastizitat poröser medien: Vierteljahrsschrift der Naturforschenden Gesellschaft in Zürich, **96**, 1–23.

Glubokovskikh, S., B. Gurevich, and N. Saxena, 2016, A dual-porosity scheme for fluid/solid substitution: Geophysical Prospecting, **64**, 1112–1121, doi: 10.1111/1365-2478.12389.

Gurevich, B., D. Makarynska, O. B. de Paula, and M. Pervukhina, 2010, A simple model for squirt-flow dispersion and attenuation in fluid-saturated granular rocks: Geophysics, **75**, no. 6, N109–N120, doi: 10.1190/1.3509782.

Gurevich, B., D. Makarynska, and M. Pervukhina, 2009, Ultrasonic moduli for fluid-saturated rocks: Mavko-Jizba relations rederived and generalized: Geophysics, **74**, no. 4, N25–N30, doi: 10.1190/1.3123802.

Hashin, Z., 1970, Complex moduli of viscoelastic composites — I. General theory and application to particulate composites: International Journal of Solids and Structures, **6**, 539–552, doi: 10.1016/0020-7683(70)90029-6.

Jakobsen, M., and M. Chapman, 2009, Unified theory of global flow and squirt flow in cracked porous media: Geophysics, **74**, no. 2, WA65–WA76, doi: 10.1190/1.3078404.

Jänicke, R., B. Quintal, and H. Steeb, 2015, Numerical homogenization of mesoscopic loss in poroelastic media: European Journal of Mechanics — A/Solids, **49**, 382–395, doi: 10.1016/j.euromechsol.2014.08.011.

Kachanov, M., and I. Sevostianov, 2018, Micromechanics of materials, with applications: Springer, 249.

Landau, L., and E. Lifshitz, 1959, Course of theoretical physics. Vol. 6: Fluid mechanics: Elsevier.

Lissa, S., N. D. Barbosa, E. Caspari, Y. Alkhimenkov, and B. Quintal, 2020, Squirt flow in cracks with rough walls: Journal of Geophysical Research: Solid Earth, **125**, e2019JB019235, doi: 10.1029/2019JB019235.

Lissa, S., M. Ruf, H. Steeb, and B. Quintal, 2021, Digital rock physics applied to squirt flow: Geophysics, **86**, no. 4, MR235–MR245, doi: 10.1190/geo2020-0731.1.

Mavko, G., and D. Jizba, 1991, Estimating grain-scale fluid effects on velocity dispersion in rocks: Geophysics, **56**, 1940–1949, doi: 10.1190/1.1443005.

Mavko, G., and A. Nur, 1975, Melt squirt in the asthenosphere: Journal of Geophysical Research, **80**, 1444–1448, doi: 10.1029/JB080i011p01444.

Morozov, I. B., and W. Deng, 2018, Elastic potential and pressure dependence of elastic moduli in fluid-saturated rock with double porosityelastic potential for porous rock: Geophysics, **83**, no. 4, MR231–MR244, doi: 10.1190/geo2016-0646.1.

Mukerji, T., and G. Mavko, 1994, Pore fluid effects on seismic velocity in anisotropic rocks: Geophysics, **59**, 233–244, doi: 10.1190/1.1443585.

Müller, T. M., B. Gurevich, and M. Lebedev, 2010, Seismic wave attenuation and dispersion resulting from wave-induced flow in porous rocks — A review: Geophysics, **75**, no. 5, 75A147–75A164, doi: 10.1190/1.3463417.

Murphy, W. F., K. W. Winkler, and R. L. Kleinberg, 1986, Acoustic relaxation in sedimentary rocks: Dependence on grain contacts and fluid saturation: Geophysics, **51**, 757–766, doi: 10.1190/1.1442128.

Nemat-Nasser, S., and M. Hori, 2013, Micromechanics: Overall properties of heterogeneous materials: Elsevier.

O'Connell, R., and B. Budiansky, 1978, Measures of dissipation in viscoelastic media: Geophysical Research Letters, **5**, 5–8.

O'Connell, R. J., and B. Budiansky, 1977, Viscoelastic properties of fluid-saturated cracked solids: Journal of Geophysical Research, **82**, 5719–5735, doi: 10.1029/JB082i036p05719.

Palmer, I., and M. Traviolia, 1980, Attenuation by squirt flow in undersaturated gas sands: Geophysics, **45**, 1780–1792, doi: 10.1190/1.1441065.

Pimienta, L., J. Fortin, and Y. Guéguen, 2015a, Bulk modulus dispersion and attenuation in sandstones: Geophysics, **80**, no. 2, D111–D127, doi: 10.1190/geo2014-0335.1.

Pimienta, L., J. Fortin, and Y. Guéguen, 2015b, Experimental study of Young's modulus dispersion and attenuation in fully saturated sandstones: Geophysics, **80**, no. 5, L57–L72, doi: 10.1190/geo2014-0532.1.

Pride, S. R., J. G. Berryman, and J. M. Harris, 2004, Seismic attenuation due to wave-induced flow: Journal of Geophysical Research: Solid Earth, **109**, B01201, doi: 10.1029/2003JB002639.

Quintal, B., E. Caspari, K. Holliger, and H. Steeb, 2019, Numerically quantifying energy loss caused by squirt flow: Geophysical Prospecting, **67**, 2196–2212, doi: 10.1111/1365-2478.12832.

Quintal, B., J. G. Rubino, E. Caspari, and K. Holliger, 2016, A simple hydromechanical approach for simulating squirt-type flow: Geophysics, **81**, no. 4, D335–D344, doi: 10.1190/geo2015-0383.1.

Shapiro, S. A., 2003, Elastic piezosensitivity of porous and fractured rocks: Geophysics, **68**, 482–486, doi: 10.1190/1.1567215.

Subramaniyan, S., B. Quintal, C. Madonna, and E. H. Saenger, 2015, Laboratory-based seismic attenuation in fontainebleau sandstone: Evidence of squirt flow: Journal of Geophysical Research: Solid Earth, **120**, 7526–7535, doi: 10.1002/2015JB012290.

Sun, C., G. Tang, J. Fortin, J. V. Borgomano, and S. Wang, 2020, Dispersion and attenuation of elastic wave velocities: Impact of microstructure heterogeneity and local measurements: Journal of Geophysical Research: Solid Earth, **125**, e2020JB020132, doi: 10.1029/2020JB020132.

Tsai, H.-C., and C.-C. Lee, 1998, Compressive stiffness of elastic layers bonded between rigid plates: International Journal of Solids and Structures, **35**, 3053–3069, doi: 10.1016/S0020-7683(97)00355-7.

Xu, S., 1998, Modelling the effect of fluid communication on velocities in anisotropic porous rocks: International Journal of Solids and Structures, **35**, 4685–4707, doi: 10.1016/S0020-7683(98)00090-0.

Zhang, Y., L. Song, M. Deffenbaugh, and M. N. Toksöz, 2010, A finite difference method for a coupled model of wave propagation in poroelastic materials: The Journal of the Acoustical Society of America, **127**, 2847–2855, doi: 10.1121/1.3372640.

Zhang, Y., and M. N. Toksöz, 2012, Computation of dynamic seismic responses to viscous fluid of digitized three-dimensional Berea sandstones with a coupled finite-difference method: The Journal of the Acoustical Society of America, **132**, 630–640, doi: 10.1121/1.4733545.

Biographies and photographs of the authors are not available.